Journal of Aerosol Science 78 (2014) 55–70

Contents lists available at ScienceDirect

Journal of Aerosol Science

journal homepage: www.elsevier.com/locate/jaerosci

# Growth rates of atmospheric molecular clusters based on appearance times and collision–evaporation fluxes: Growth by monomers

Tinja Olenius [a,*], Ilona Riipinen [b], Katrianne Lehtipalo [a,c], Hanna Vehkamäki [a]

[a] Department of Physics, University of Helsinki, Gustaf Hällströmin katu 2 A, P.O. Box 64, FIN-00014 Helsinki, Finland
[b] Department of Applied Environmental Science and Bolin Centre for Climate Research, Stockholm University, SE-10691 Stockholm, Sweden
[c] Airmodus Oy, Pietari Kalmin katu 1 F 1, FI-00560 Helsinki, Finland

ARTICLE INFO

*Article history:*
Received 30 April 2014
Received in revised form
26 August 2014
Accepted 26 August 2014
Available online 16 September 2014

*Keywords:*
Growth rate
Molecular cluster
Data analysis
Critical cluster
New particle formation

ABSTRACT

Formation of secondary atmospheric aerosol particles starts with the formation and growth of small molecular clusters. The probability that freshly formed clusters reach larger sizes depends on the rate at which they grow with respect to the rate at which they are lost on pre-existing surfaces. At present, advances in condensation particle counter and mass spectrometer techniques enable the observation of cluster growth via time evolution of size resolved cluster concentrations, and recent studies have utilized measured concentrations to deduce growth rates from the appearance times of different cluster sizes. In this work, we use a dynamic model to simulate the time development of a population of clusters of up to ~2 nm in mass diameter, and examine the relation of the growth rates determined from the appearance times to the growth rates calculated from the molecular fluxes between the clusters. This study concentrates on a simple model substance where the clusters grow only by monomer additions and the growth involves a single free energy barrier. Each cluster size defined by the number of molecules in the cluster is explicitly treated instead of dividing the clusters into size classes. Effects of finite size resolution and cluster–cluster collisions will be discussed in future work. We find that the growth rates determined with the two different approaches may differ significantly, both quantitatively and qualitatively, for the smallest clusters with the highest evaporation rates. The relative difference decreases with increasing cluster size and decreasing evaporation rate. In addition to cluster size, the difference depends on ambient conditions including external losses and time profile of the monomer concentration. Thus a quantitative comparison requires information not only on the substance, but also on the external conditions. We also show that the size of a critical cluster, corresponding to the maximum of an energy barrier in cluster formation, cannot be inferred from the size-dependent growth rates in realistic conditions.



## 1. Introduction

The first steps of atmospheric new particle formation process involve clustering of individual molecules and growth of the clusters by collisions with gas-phase molecules and each other. Aerosol particle concentrations are ultimately limited by

* Corresponding author. Tel.: +358 50 415 4740.
*E-mail address:* tinja.olenius@helsinki.fi (T. Olenius).

http://dx.doi.org/10.1016/j.jaerosci.2014.08.008
0021-8502/

the formation rate of the initial molecular clusters, but the survival probability of freshly formed particles to larger sizes depends on the rates at which the particles grow and are lost on pre-existing larger particles or surfaces (Kerminen et al., 2001; Kuang et al., 2010). The time evolution of particle size distribution during a new particle formation event can be described considering these competing processes. The time derivative of particle concentration $C_{D_p}$ in a size class with a mean particle diameter $D_p$ and a width of $\Delta D_p$ is (see, for example, Sihto et al., 2006; Kulmala et al., 2012)

$$\frac{dC_{D_p}}{dt} = J_{D_p} - \frac{GR_{D_p}}{\Delta D_p} C_{D_p} - S_{D_p}, \quad (1)$$

where $J_{D_p}$ is the formation rate of particles in the size range, $GR_{D_p}$ is the growth rate of the particles to larger sizes (as the change of particle diameter per unit time), and $S_{D_p}$ is an external loss term due to deposition onto pre-existing particles or surfaces. If the particles are formed via growth from the preceding smaller size class $D_p - \Delta D_p$, the formation rate $J_{D_p}$ equals to the growth term of the smaller size range $J_{D_p} = GR_{D_p - \Delta D_p} C_{D_p - \Delta D_p} / \Delta D_p$, where it is assumed that the size classes have equal width $\Delta D_p$. The formation and growth terms (the first and second term on the right-hand side of Eq. (1)) include the effects of condensation and evaporation of vapor monomers, and possibly also collisions and fragmentations involving two clusters.

The growth rates of freshly formed particles of a few nanometers and upwards in diameter are in general deduced from measured particle concentrations during new particle formation events (Manninen et al., 2009, 2010; Yli-Juuti et al., 2011 and references therein), or calculated based on concentrations of condensable vapors (Nieminen et al., 2010; Yli-Juuti et al., 2013) and sometimes also coagulation (Stolzenburg et al., 2005; Leppä et al., 2011). The most widely used approaches to obtain the growth rates from experimental data include the mode fitting method (Dal Maso et al., 2005) and the maximum concentration method (Hirsikko et al., 2005). Another approach is to retrieve the growth rates from the time delay between the rise of concentrations measured with several particle counters with different detection threshold sizes (Riccobono et al., 2012). The time lag between the appearance of different sized particles has also been studied analytically (Wu, 1992 and references therein). Growth rates can also be determined by fitting analytical equations of the form of Eq. (1) to the time-dependent particle distribution data (Verheggen & Mozurkewich, 2006; Lehtinen et al., 2004; Kuang et al., 2012). Earlier, instrumental detection limit has restricted the determination of growth rates to particle sizes larger than a couple of nanometers in mobility diameter. Growth rates of particles below the detection limit have been estimated from the time lag between the increase in sulfuric acid concentration and the concentration of the smallest detected particles (Weber et al., 1997; Fiedler et al., 2005; Sihto et al., 2006). At present, condensation particle counters observe particles and molecular clusters down to the mobility diameter of 1 nm (Jiang et al., 2011; Vanhanen et al., 2011; Kulmala et al., 2013), and individual charged clusters can be detected and identified by high-resolution mass spectrometry (Junninen et al., 2010; Schobesberger et al., 2013). The growth rates of the smallest clusters can be likewise defined from the measured concentration time series. However, for example in chamber experiments with a constant vapor source, the cluster concentrations may increase to the steady state monotonously without exhibiting a maximum in which case methods based on determining the moment of the maximum concentration cannot be applied. Hence, in recent studies the growth rates have been determined based on cluster appearance times, generally defined as the time at which the concentration of the cluster reaches 50% of its maximum value (which may or may not equal to the steady-state value) or sometimes 50% of the total increase in the concentration in the case that there is a background level before the beginning of particle formation (Kulmala et al., 2013; Schobesberger et al., 2013; Lehtipalo et al., 2014; Wimmer et al., 2014). Alternative definitions for the appearance time have been tested by Lehtipalo et al. (2014). The appearance time method has been applied to simulation data from a condensation–coagulation aerosol microphysics model, and the results were found to roughly agree with the average condensational growth rates of different particle size classes (Lehtipalo et al., 2014).

From a theoretical perspective, the growth rates of the smallest clusters cannot be determined assuming irreversible vapor condensation or cluster coagulation, as also evaporation of molecules may be significant for the small sizes (Ortega et al., 2012; Yli-Juuti et al., 2013). In the case that the formation free energy profile of the growing clusters contains one global maximum corresponding to the critical cluster, the relative effect of evaporation with respect to growth by collisions is the most significant for clusters below the critical size. For clusters larger than the critical size, evaporation becomes less significant as the cluster size increases. It has been speculated that the critical size may be identifiable from observed cluster growth rates by rationalizing that evaporation substantially decreases the growth rate of sub-critical clusters, whereas at the critical size the growth rate starts to increase due to cluster stabilization. The critical size regime has thus been assessed by comparing measured growth rates to theoretical growth rates calculated assuming only vapor condensation and no evaporation (Kuang et al., 2012; Kulmala et al., 2013).

In this study we use a dynamic model to simulate the time evolution of a cluster population in a one-component system. We use a model substance that exhibits a critical cluster size, with the properties mimicking atmospherically relevant stabilized clusters. The cluster growth rates are determined from the simulation data with two different methods. First, we apply the experimental data analysis method to the simulated cluster concentration time series to extract the growth rates from the cluster appearance times in the same way as they are obtained from measurements. Second, we calculate the growth rates from the simulated collision–evaporation fluxes between different cluster sizes. The results give information on the qualitative relation between the effective growth rate calculated from the molecular fluxes that cannot be directly measured, and the apparent growth rate that can be deduced from cluster measurements. In addition, we examine the

growth rate as a function of cluster size, and investigate the possibility of inferring the critical size from the size dependency of the growth rate.

We concentrate on an ideal situation where the cluster growth proceeds via monomer additions and the growth pathway exhibits a free energy barrier corresponding to a critical cluster. We also assume that the time-dependent concentration can be recorded separately for each cluster; that is, the cluster size can be determined with the ideal precision of one molecule, and thus the clusters do not need to be grouped into wider size classes. The questions of finite size resolution and growth that involves collisions with small clusters will be discussed in a future study. We examine the effect of external factors, namely the magnitude of external cluster sinks and the time evolution of the vapor concentration, on the growth rates determined with the two methods as well as their relation. The presented case studies correspond to conditions typical to chamber or field measurements. The focus of this work is on the qualitative behavior of these two quantities as a function of cluster size in varying conditions; quantitative predictions require information on the properties of the specific substance of interest and on the external parameters.

## 2. Methods for determining cluster growth rates

The appearance time method, first implemented by Kulmala et al. (2013) and introduced in detail by Lehtipalo et al. (2014), is currently used for experimentally determining the growth rates of the smallest atmospheric molecular clusters of approximately 1–2 nm in mobility diameter. A theoretical approach to obtain the cluster growth rate is to calculate the flux of molecules onto the cluster taking into account condensation and evaporation of vapor molecules, and possibly also smaller molecular clusters.

In atmospheric particle measurements, the observed particles or clusters are most often classified according to their mobility diameter, and thus the growth rate of a particle is normally given as the change in particle diameter per unit time (normally in nm $h^{-1}$). The mobility diameter is often approximated as 0.3 nm larger than the mass diameter (Larriba et al., 2011), but it must be noted that this approximation is not generally valid for all substances (Ouyang et al., 2013), especially in the case of very small particles. In this work we use the mass diameter which can be unambiguously determined for spherical particles. The growth rate can as well be given as the change in particle mass or number of molecules, which can be converted to the change in diameter assuming spherical particles, provided that the density of the substance is known. The latter case is relevant, for instance, if the particles are observed with a mass spectrometer. The qualitative behavior of the growth rate curve as a function of cluster size depends on which physical quantity is used to characterize the cluster size, as the diameter of a spherical cluster is proportional to the third root of the cluster mass. Therefore, in this study, the cluster growth rates are given both as the change in the number of molecules in the cluster, and as the change in the mass diameter of the cluster, assuming spherical clusters.

### 2.1. Appearance times of the clusters

The appearance time method (Kulmala et al., 2013; Schobesberger et al., 2013; Lehtipalo et al., 2014; Wimmer et al., 2014) is based on the time evolution of particle concentrations during a new particle formation event. The concentration of each different cluster or particle size, or in practice size class, is recorded as a function of time. The appearance time $t_{app}$ of each particle size $D_p$ is determined as the time at which the concentration reaches 50% of its maximum value. In the case of a non-zero initial concentration, the appearance time is in this work determined as the time at which the concentration reaches 50% of the total increase in the concentration (maximum value minus initial value; Schobesberger et al., 2013). The diameter $D_p$ of the observed particles is then presented as a function of appearance time, and the growth rate is determined as the slope of a linear fit to the ($t_{app}$, $D_p$)-data. If the relation between the diameter and the appearance time is not linear throughout the particle size range, several fits can be made separately to different size ranges to obtain a different growth rate for each size class, as done by Kulmala et al. (2013) and Lehtipalo et al. (2014).

In this study, the growth rate derived from the appearance times is determined from the ($t_{app}$, $D_p$)-curve separately for each pair of adjacent clusters $i$ and $i+1$ as

$$\mathrm{AGR}_i \equiv \frac{\Delta D_{p,i\to i+1}}{\Delta t_{app,i\to i+1}} = \frac{D_{p,i+1} - D_{p,i}}{t_{app,i+1} - t_{app,i}}, \tag{2}$$

where $i$ refers to the cluster containing $i$ molecules, and the abbreviation AGR refers to appearance time-based growth rate. It should be emphasized that this definition is well-founded in the case that the cluster growth occurs in practice solely due to monomer additions.

### 2.2. Molecular fluxes to the clusters

From theoretical point of view, the growth rate of a cluster can be determined from the frequency at which the cluster gains molecules. This is normally done by calculating the volume change rate of a spherical particle of a specific diameter considering condensation of surrounding vapors and possibly also evaporation of molecules from the surface of the particle (Fuchs & Sutugin, 1970; Riccobono et al., 2012; Yli-Juuti et al., 2013). This so-called Lagrangian representation, however, cannot be applied to study the growth of very small molecular clusters for which evaporation is significant, as shown below.

Instead, we present here a slightly different approach based on the net flux between consecutive cluster sizes, referred to as the Eulerian approach. Below we briefly summarize the concepts of the traditional Lagrangian approach, and present the Eulerian approach used in this work. The molecular flux-based growth rates presented here can always be calculated from the cluster concentrations, provided that the collision and evaporation rate coefficients are known. The derivations in Sections 2.2.1 and 2.2.2 are for a one-component system where the clusters grow and decay via monomer additions and evaporations. For systems in which also small clusters contribute to the growth, defining the cluster growth rate is less straightforward and will be discussed in a future study.

*2.2.1. Lagrangian approach*

Let us consider a spherical cluster consisting of $i$ molecules that grows by collisions with monomers, and also loses molecules by monomer evaporation. Hence the rate at which the cluster volume $V_i$ changes can be written as

$$\frac{dV_i}{dt} = (\beta_{i,1} C_1 - \gamma_{i\to i-1})\frac{m_1}{\rho}, \tag{3}$$

where $\beta_{i,1}$ is the collision rate coefficient between cluster $i$ and a monomer, $C_1$ is the concentration of monomers, $\gamma_{i\to i-1}$ is the evaporation rate coefficient of cluster $i$ into cluster $i-1$, $m_1$ is the mass of a monomer, and $\rho$ is the density of the clusters. Consequently, the change rate of the cluster mass diameter $D_{p,i}$ can be written as

$$\frac{dD_{p,i}}{dt} = \frac{dD_{p,i}}{dV_i}\frac{dV_i}{dt} = \frac{6}{3\pi D_{p,i}^2}(\beta_{i,1} C_1 - \gamma_{i\to i-1})\frac{m_1}{\rho} = \left(\frac{6m_1}{\pi\rho}\right)^{1/3}\frac{1}{3i^{2/3}}(\beta_{i,1} C_1 - \gamma_{i\to i-1}), \tag{4}$$

where the last equality is obtained by writing the diameter as $D_{p,i} = \left[6m_1 i/(\pi\rho)\right]^{1/3}$.

*2.2.2. Eulerian approach*

Instead of observing the growth of a specific cluster, let us now study the flux between two adjacent cluster sizes, again assuming that the cluster growth involves only monomer additions and evaporations. If cluster $i$ grows by monomer collisions, and the resulting cluster of $i+1$ molecules may also evaporate back into cluster $i$, the net flux between clusters $i$ and $i+1$ is

$$I_{i,i+1} = \beta_{i,1} C_1 C_i - \gamma_{i+1\to i} C_{i+1}, \tag{5}$$

where $C_i$ is the concentration of cluster $i$. Now, taking into account the backwards evaporation flux, cluster $i$ grows in the direction of cluster $i+1$ at the frequency

$$f_{i,i+1} = \frac{I_{i,i+1}}{C_i} = \beta_{i,1} C_1 - \gamma_{i+1\to i}\frac{C_{i+1}}{C_i}. \tag{6}$$

The diameter growth rate of cluster $i$ can then be calculated as

$$\frac{dD_{p,i}}{dt} = (D_{p,i+1} - D_{p,i}) f_{i,i+1} = \left(\frac{6m_1}{\pi\rho}\right)^{1/3}\left[(i+1)^{1/3} - i^{1/3}\right]\left(\beta_{i,1} C_1 - \gamma_{i+1\to i}\frac{C_{i+1}}{C_i}\right). \tag{7}$$

Approximating the diameter change $D_{p,i+1} - D_{p,i}$ in Eq. (7) by $dD_{p,i}/di$ results in the same pre-factor $\left[6m_1/(\pi\rho)\right]^{1/3}[1/(3i^{2/3})]$ as in the Lagrangian representation (Eq. (4)). The pre-factor values given by the approximation $dD_{p,i}/di$ approach the values obtained with the accurate expression $D_{p,i+1} - D_{p,i}$ very rapidly as the cluster size increases; for the monomer, the difference compared to the accurate value is 28%, and for clusters larger than 10 molecules, the deviation is less than 3%.

The essential difference between the diameter growth rates given by Eqs. (4) and (7), obtained with the Lagrangian and Eulerian approaches, respectively, is the evaporation term included in the last factor which corresponds to the frequency at which the cluster gains molecules. The Lagrangian perspective should be used when following the growth of an individual cluster between different size classes. On the other hand, if the growth rate is used in calculating the time evolution of particle concentrations as presented in Eq. (1), the consistent approach is the Eulerian representation: as the growth term in Eq. (1) corresponds to the net flux $I_{D_p,\, D_p+\Delta D_p}$ from size class $D_p$ to the adjacent size class $D_p+\Delta D_p$

$$\frac{GR_{D_p}}{\Delta D_p} C_{D_p} = I_{D_p,\, D_p+\Delta D_p},$$

the growth rate equals to

$$GR_{D_p} = \Delta D_p \frac{I_{D_p,\, D_p+\Delta D_p}}{C_{D_p}}.$$

This corresponds to the Eulerian growth rate definition given by Eq. (7). Furthermore, the Lagrangian method is not an intuitive approach for a system containing a critical cluster (see Section 3.1). Clusters smaller than the critical size are, by definition, more likely to evaporate than to grow, in other words their evaporation frequency $\gamma_{i\to i-1}$ is higher than their collision frequency with monomers $\beta_{i,1} C_1$. Hence the Lagrangian approach (Eq. (4)) results in negative growth rates for all sub-critical clusters, although there is a positive net flux through the system during a new particle formation event. Therefore we use the Eulerian method to determine the theoretical cluster growth rate and abbreviate it as FGR, referring to

flux-equivalent growth rate. Eq. (7) gives the growth rate as the change in diameter per unit time. The growth rate as the change in number of molecules per unit time is calculated by replacing the difference in the diameters $D_{p,i+1}-D_{p,i}$ with the difference in the numbers of molecules, that is, one molecule in the case of growth by monomer additions.

## 3. Cluster dynamics simulations

The time evolution of a cluster population in a one-component system was simulated using the dynamic cluster model Atmospheric Cluster Dynamics Code (ACDC; McGrath et al., 2012; Olenius et al., 2013). The code generates the time derivatives of the concentrations of a given system of clusters, and solves the time-dependent cluster concentrations numerically using the Matlab ode15s solver (Shampine & Reichelt, 1997). The time derivatives, also known as the birth–death equations, include all possible collision and evaporation processes between all clusters of the studied system. The birth–death equations can be set to include also external sink terms. For a one-component substance with the critical cluster inside the simulation system, clusters that grow beyond the largest cluster size studied are considered to be stable and are removed from the simulation. The vapor monomer concentration is either set to a fixed constant or time-dependent value, or solved from the differential equations after giving a fixed monomer source rate and initial concentration. To obtain a realistic time resolution for determining the appearance times of the clusters, the maximum time step of the differential equation solver was set to 1 s.

### 3.1. Model substance and simulation conditions

The initial clustering is often driven by sulfuric acid (Kuang et al., 2008 and references therein) and enhanced by other compounds such as bases and organic species (Zhang et al., 2004; Yu et al., 2012; Almeida et al., 2013; Schobesberger et al., 2013), with the subsequent growth dominated by organic compounds (Pierce et al., 2011; Yli-Juuti et al., 2011; Riipinen et al., 2012). The exact identities of the compounds participating in the process in different locations remain unknown. Thus we have chosen a model substance that can be seen as a quasi-unary representation of a multi-component system relevant to atmospheric cluster formation. The clusters in the studied system consist of molecules with a mass of $m_1=98.08$ amu, a liquid density of $\rho=1830\ \mathrm{kg\ m^{-3}}$ and a surface tension of $\sigma=0.05\ \mathrm{N\ m^{-1}}$, which correspond to the properties of sulfuric acid, but a saturation vapor pressure of $P_{sat}=10^{-9}$ Pa, which is significantly lower than that of sulfuric acid (see below) at a constant temperature of 278 K. The simulations include clusters containing up to 70 molecules (corresponding to a mass diameter of 2.3 nm with the used mass and density), with additional test runs performed with a system including clusters with up to 30 and 50 molecules to ensure that the boundary effects are restricted to the few largest clusters at the system boundary (see Section 4).

The collision rate coefficients are calculated based on kinetic theory of gases from the mass and density of the model substance assuming spherical clusters. The evaporation rate coefficients are obtained from the Gibbs free energies of formation of the clusters according to the condition of detailed balance (see, for example, Ortega et al., 2012). It must be noted that for real substances, quantitative rate coefficients may differ from hard-sphere collision rates and evaporation rates calculated from an equilibrium situation. The behavior of the rate constants as a function of cluster size calculated using these approximations is likely to be realistic, and thus the model system allows the assessment of the qualitative coherence of the two different growth rate definitions.

The Gibbs free energy of formation for each cluster is calculated according to the classical one-component liquid droplet model:

$$\Delta G_i = -(i-1)k_B T \ln S + (A_i - A_1)\sigma, \tag{8}$$

where $i$ is the number of molecules in the cluster, $S$ is the saturation ratio, $k_B$ is the Boltzmann constant, $T$ is the temperature, and $A_i$ is the surface area of cluster $i$. The simulations were generally performed with the final or maximum saturation ratio set to $S=20$, 30 and 40, which correspond to critical cluster sizes of $i^*=24$, 16 and 13 molecules, respectively. The free energy curves are presented in Fig. 1a. The saturation ratio is connected to the monomer vapor concentration $C_1$ via the ideal gas law as $C_1 = SP_{sat}/(k_B T)$, where $P_{sat}$ is the saturation vapor pressure. To produce atmospherically relevant monomer concentrations corresponding to the saturation ratios $S=20$, 30 and 40 that we used to calculate the different Gibbs free energy of formation curves, the saturation vapor pressure of the model substance was set to $10^{-9}$ Pa. This results in concentrations $C_1=5.2\times10^6\ \mathrm{cm^{-3}}$, $7.8\times10^6\ \mathrm{cm^{-3}}$ and $1.0\times10^7\ \mathrm{cm^{-3}}$, respectively, which correspond to sulfuric acid concentrations typical for atmospheric new particle formation. It must be noted that while the Gibbs free energies of the clusters that are calculated according to Eq. (8) are independent of the saturation vapor pressure, the cluster evaporation rates that are calculated using the detailed balance are directly proportional to it. The value used for $P_{sat}$ combined with the Gibbs free energies (Eq. (8)) results in monomer evaporation rates of the order of magnitude of $10^{-3}$–$10^{-2}\ \mathrm{s^{-1}}$ (Fig. 1b), which are in the range of evaporation rates calculated from quantum chemical formation free energies for small sulfuric acid–base clusters (Ortega et al., 2012). It must be noted that while simulations performed with the model substance give qualitative information on cluster growth in a system with the classical free energy profile, obtaining quantitative results for a specific substance requires information on the properties of the molecules and clusters of interest.

The simulations were run at a temperature of 278 K. The vapor monomer was set to have either a fixed concentration or a fixed source rate, and the simulations were performed with or without external loss terms, as described in more detail in

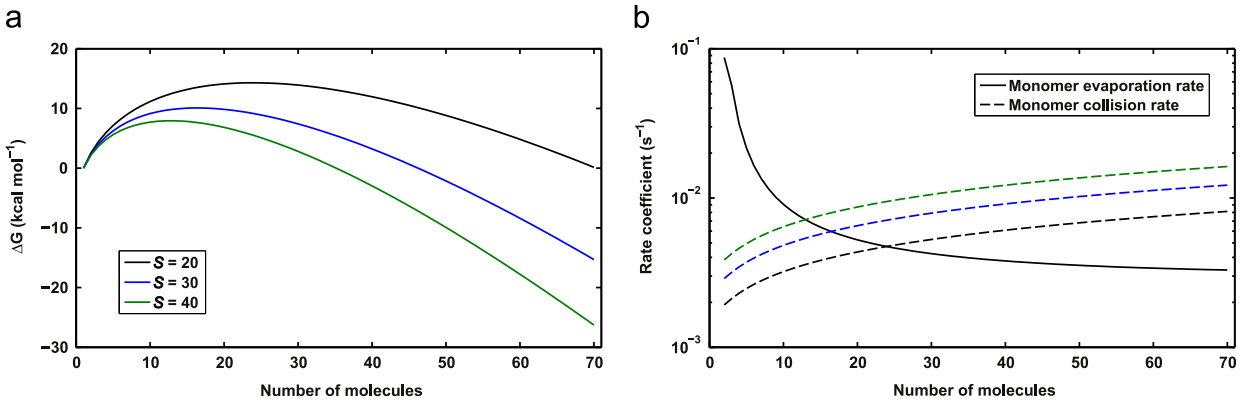


**Fig. 1.** Panel (a): Gibbs free energy of formation from monomers as a function of number of molecules in the cluster in the studied one-component system at saturation ratios $S=20$ (black), 30 (blue) and 40 (green). Panel (b): Evaporation rate of monomers from the cluster calculated from the Gibbs free energies (solid line). Collision rate of monomers at $S=20$, 30 and 40 is also shown for reference (dashed black, blue and green lines, respectively). The evaporation and collision rates coincide at the critical cluster size located at the maximum of the formation free energy curve. (For interpretation of the references to color in this figure legend, the reader is referred to the web version of this article.)

Section 4. In the case of simulations with a constant monomer source rate, the source rate was ensured to be high enough to result in a cluster appearance time period that is not longer than a few hours.

### 3.2. *Effect of cluster–cluster collisions*

To calculate the growth rate from the molecular fluxes $I$ as described in Section 2.2.2, the clustering pathways must be known. As the determination of growth rates using Eqs. (2) and (7) requires that the clustering occurs solely by monomer additions, the used model substance needs to satisfy this condition. Disabling collisions of clusters is not justifiable in the case that their concentrations are actually high enough to contribute to the growth. Therefore the growth pathways in a simulation where cluster–cluster collisions and evaporations are allowed were examined in order to ensure that forbidding cluster–cluster processes does not have a significant effect on the results. Growth by small clusters (mostly by dimers) was found to form at most 1–3% of the total flux from the clusters (although for the smallest clusters containing less than circa five molecules, the fraction could be over 10% in the hypothetical system of Section 4.1), and therefore the cluster–cluster processes can be neglected in this work. Thus from now on, the discussion concentrates on the case where only monomer processes occur.

## 4. Results and discussion

In the studied conditions, the cluster concentrations increased smoothly to the final steady-state value, which thus equals the maximum concentration from which the appearance times are determined. The system boundary effects become visible around sizes where the clusters contain more than approximately 65 molecules: clusters that are near the boundary of the system have artificially high growth fluxes as there are no evaporation fluxes back into the simulated system from clusters that have grown out from it. Thus the results are shown only for clusters with up to 65 molecules.

Sections 4.1 and 4.2 present case studies carried out in different simulation conditions. Section 4.1 focuses on a theoretical case where the monomer concentration is constant and there are no external losses, and Section 4.2 concentrates on a more realistic situation with varying monomer production rates and loss terms. For clarity, the growth rates determined from the appearance times (Eq. (2)) are referred to as $\mathrm{AGR}_N$ or $\mathrm{AGR}_{D_\mathrm{p}}$, and the growth rates calculated from the molecular fluxes (Eq. (7)) are referred to as $\mathrm{FGR}_N$ or $\mathrm{FGR}_{D_\mathrm{p}}$, where subscripts $N$ and $D_\mathrm{p}$ refer to growth rates given as the change in the number of molecules in the cluster and as the change in the mass diameter of the cluster, respectively. For each cluster size $i$, the flux-based growth rate FGR was calculated both at the steady state and at the mean appearance time of cluster $i$ and the subsequent cluster $i+1$, denoted as $t_{\mathrm{app,\ mean}} \equiv (t_{\mathrm{app},\ i} + t_{\mathrm{app},\ i+1})/2$.

### 4.1. *Constant monomer concentration and no external losses*

In the first set of simulations, the monomer concentration was set to a constant value corresponding to different saturation ratios, while the initial concentrations of all other clusters were set to zero. External loss terms were not used. Panel (a) of Fig. 2 shows the cluster size versus its appearance time, and panel (b) presents the growth rate as a function of cluster size determined with the two different methods. The solid lines show the apparent growth rate AGR, defined as the slope $\Delta\mathrm{size}/\Delta t_{\mathrm{app}}$ of the appearance time curves shown in panel (a) (Eq. (2)). The lines with symbols present the growth rate FGR calculated from the molecular fluxes (Eq. (7)) at the end of the simulation when the system has reached the steady

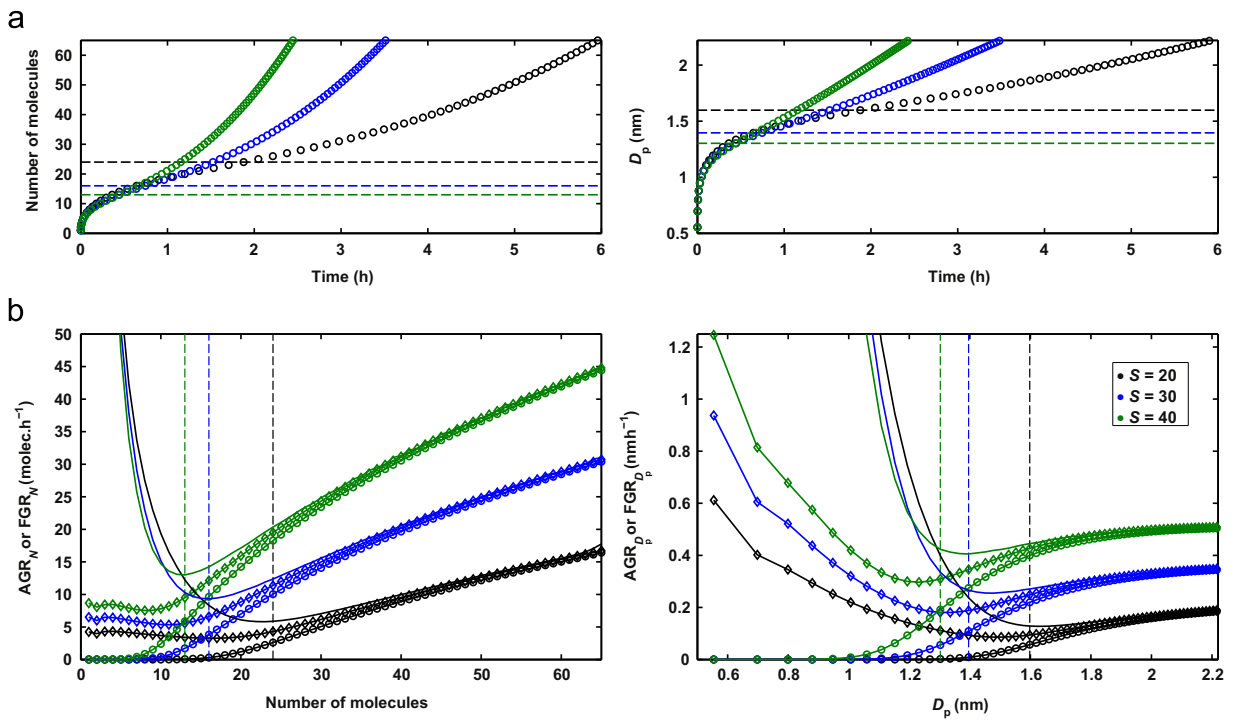


**Fig. 2.** Results for simulations with a constant monomer concentration corresponding to saturation ratios $S=20$ (black), 30 (blue) and 40 (green) and no external losses. Panel (a): Cluster size as a function of appearance time. Panel (b): Cluster growth rate (1) determined as the slope of cluster size as a function of appearance time (AGR; solid lines), and (2) calculated from the net molecular flux onto the cluster (FGR) as a function of cluster size at the steady-state (lines with circles) and at the appearance time $t_{app,\ mean}$ (lines with diamonds). Dashed lines mark the size of the critical cluster for the different saturation ratios. Cluster size and growth rate are given as the number of molecules in the left-hand panels, and as the mass diameter in the right-hand panels. (For interpretation of the references to color in this figure legend, the reader is referred to the web version of this article.)

state (circles), and at the mean appearance time $t_{app,\ mean}$ of the consecutive clusters (diamonds). The size of the critical cluster for each saturation ratio is marked with a dashed line.

The time difference $\Delta t_{app}$ between the appearance of clusters of adjacent sizes first increases with size until the sizes around the critical cluster are reached, and then decreases towards larger sizes (panel (a)). Correspondingly, AGR (solid lines in panel (b)) first decreases and then increases. For each saturation ratio, the location of the minimum in AGR is relatively close to the critical size (dashed lines), but does not necessarily coincide with it. The behavior of AGR is related to the fact that the evaporation fluxes towards the smallest clusters are lower at the times when these clusters appear than in the final steady state, as explained below. However, it must be noted that the definition of the appearance time as the time at which the cluster concentration reaches 50% of its maximum is a matter of choice. If, for example, 10% or 90% are used instead of 50%, the location of the minimum is slightly shifted.

The molecular flux-based growth rate FGR calculated at the steady-state increases as a function of cluster size throughout the size range (lines with circles in panel (b)). FGR calculated at the mean appearance time (lines with diamonds in panel (b)) is clearly higher than the steady-state FGR for sizes smaller than the critical cluster. This can be explained by the time evolution of the net flux between clusters of consecutive sizes: at the appearance times of the smallest clusters, the concentrations of the larger clusters have not yet built up and thus evaporation fluxes from the larger sizes are lower than they are in the steady state. This is illustrated by Fig. A1 in Appendix A, which compares FGR calculated from the net fluxes, as in Fig. 2b, and FGR calculated neglecting the evaporation fluxes for a representative saturation ratio $S=30$. $FGR_{Dp}$ calculated at $t_{app,\ mean}$ exhibits a clear minimum similarly to AGR. The minimum originates from the fact that the change in cluster diameter $\Delta D_p$ related to the addition of a monomer is the largest for the smallest clusters and decreases as the cluster size increases. On the other hand, the change in the number of molecules $\Delta N$ is always one in a monomer addition, and thus there is no such a steep minimum on the $FGR_N$ curve as there is on the $FGR_{Dp}$ curve.

At sizes larger than the critical cluster, FGR determined at the steady-state and at $t_{app,\ mean}$ approach each other. This can be explained by the fact that the larger the cluster is, the closer to the final steady-state situation it appears (see Fig. A2 in Appendix A). For the larger sizes, the apparent growth rate AGR also approaches the flux-based growth rate FGR, but is always at least slightly higher than FGR throughout the cluster size range in all the simulated conditions (see Fig. A3b). For clusters larger than the critical size, the ratio of AGR and FGR approaches a value between approximately 1 and 2 for the model substance and conditions considered in this study; for smaller clusters the ratio may be more than ten times higher. It must be emphasized that since the growth rates, both AGR and FGR, are affected by cluster evaporation, also their ratio as

a function of cluster size depends on the evaporation rates. Therefore the values of the ratio are not applicable for arbitrary substances with different properties and evaporation profiles.

### 4.2. Time-dependent monomer concentration and external losses

In a realistic situation, the monomer concentration is not constant, but instead increases due to a vapor source, with the cluster concentrations increasing simultaneously. External losses of monomers and clusters onto pre-existing particles and macroscopic surfaces are also likely to be present in all real situations. Therefore, in the second set of simulations, the monomer source rate was set to constant values that result in the same set of final time-independent saturation ratios $S$ as in the first set of simulations (Section 4.1). The precursor vapor concentration is not likely to be zero between particle formation events in field or chamber experiments (Kirkby et al., 2011; Kulmala et al., 2013), and thus the initial cluster concentrations were set to a steady-state distribution at a saturation ratio of $S_{\mathrm{init}}=0.1$, which corresponds to a monomer concentration of $2.6\times10^{4}\,\mathrm{cm}^{-3}$. An external loss term with a constant loss coefficient of $10^{-3}\,\mathrm{s}^{-1}$ was used for all the clusters, corresponding to the magnitude of coagulation loss onto pre-existing larger particles in a boreal forest (Dal Maso et al., 2008). The wall loss rate coefficient for example in the CLOUD chamber experiments is reported to be of the same order of magnitude (Almeida et al., 2013). With this loss coefficient, the monomer source rates that produce the final saturation ratios $S=20$, 30 and 40 are $5.3\times10^{3}\,\mathrm{cm}^{-3}\,\mathrm{s}^{-1}$, $8.1\times10^{3}\,\mathrm{cm}^{-3}\,\mathrm{s}^{-1}$ and $1.1\times10^{4}\,\mathrm{cm}^{-3}\,\mathrm{s}^{-1}$, respectively. The results for the second set of simulations are presented in Fig. 3.

The growth rates are in general higher for the case involving an increasing monomer concentration and losses than for the case with a constant monomer concentration and no losses (Fig. 2), except for the smallest clusters, for which AGR (solid lines in Fig. 3b) and FGR calculated at the appearance times (lines with diamonds in Fig. 3b) are lower than for the simplified case discussed in Section 4.1 (for a better comparison, see Fig. A1 in Appendix A). The first term on the right-hand side of Eq. (6), corresponding to the collision flux from cluster $i$, is naturally lower in the beginning of the simulation when the monomer concentration is lower (although the decreasing effect on FGR may not be prominent; see Fig. A1). The second term, corresponding to the evaporation flux back to cluster $i$, depends on the ratio of the concentrations of clusters $i$ and $i+1$, which are affected by both the monomer concentration and the losses. The effect of the losses accumulates as the size of the cluster increases, since the concentration of cluster $i+1$ depends on the concentration of the preceding cluster $i$. Thus the losses decrease the concentrations of larger clusters relatively more than those of the smaller clusters, and consequently the ratio $C_{i+1}/C_i$ and the evaporation flux decrease for each cluster $i$. As a result, the growth rates are actually higher in the

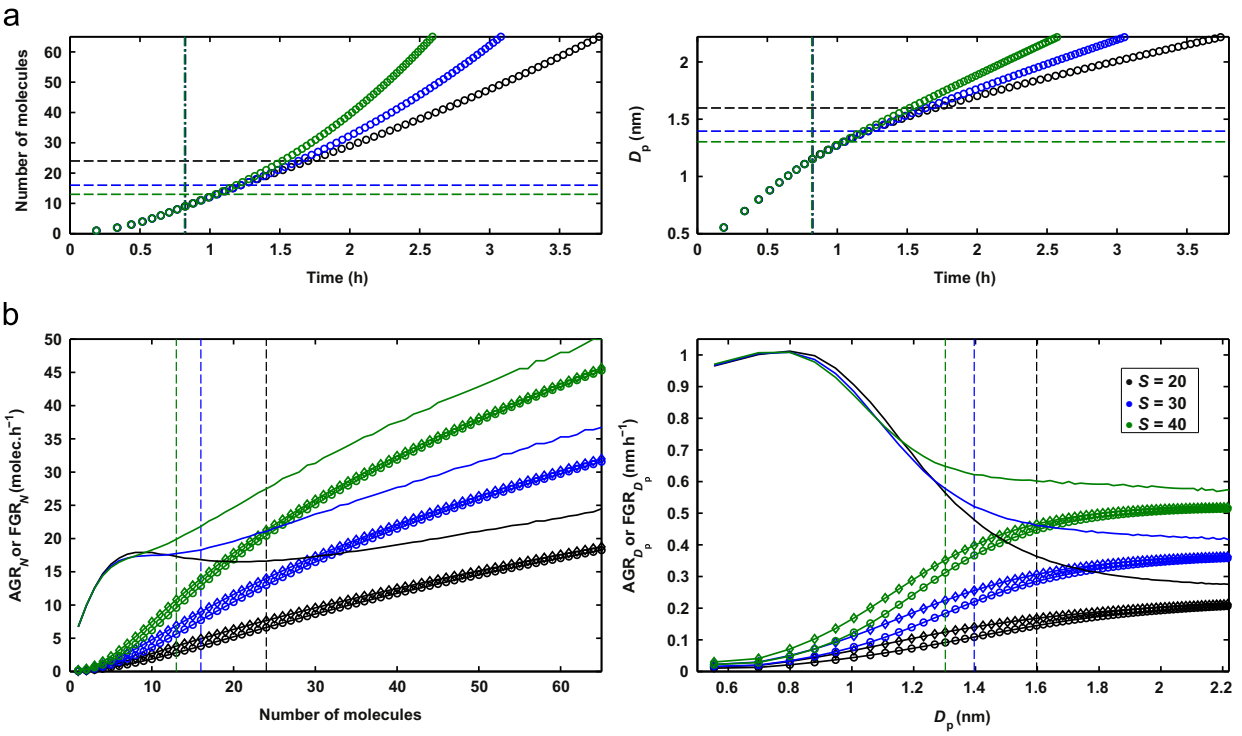


**Fig. 3.** Results for simulations with a constant monomer source rate corresponding to steady-state saturation ratios $S=20$ (black), 30 (blue) and 40 (green) and external losses with a loss coefficient of $10^{-3}\,\mathrm{s}^{-1}$. Explanations for the panels are as in Fig. 2. Dashed lines mark the size of the critical cluster at the final steady state. The dash-dotted vertical lines in panel (a) mark the time at which the monomer concentration reaches 95% of its final value (note that the lines for different saturation ratios fall on top of each other). (For interpretation of the references to color in this figure legend, the reader is referred to the web version of this article.)

presence of losses for all the clusters when the simulation has been run long enough that the monomer concentration approaches the steady-state value. On the other hand, the lower monomer concentration in the beginning of the simulation delays the appearance of the smallest clusters (panel (a) of Fig. 3), leading to the concentrations of larger cluster sizes being already higher when the smallest clusters appear compared to the hypothetical case of Section 4.1. Hence the evaporation fluxes towards the small cluster sizes at $t_{\mathrm{app,\ mean}}$ are more significant than in the case of Section 4.1, and consequently the growth rates FGR of these small clusters determined at $t_{\mathrm{app,\ mean}}$ are lower (lines with diamonds in panel (b); see also Fig. A2).

The most significant difference in the appearance time-based growth rate AGR for the first (Fig. 2) and the more realistic second (Fig. 3) set of simulations is that the existence of a critical size is no longer visible in the second simulation set. None of the solid curves in Fig. 3b exhibit a clearly distinguishable minimum. Moreover, in this case the critical size is time-dependent as it varies with the monomer concentration. For instance, for a final saturation ratio of 30, the saturation ratio is 15.1 at the appearance time of the monomer. This corresponds to a critical cluster of 32 molecules, while in the final steady state the critical size is 16 molecules. At the appearance time of clusters containing 16 molecules, which is the molecule number of the steady-state critical cluster, the saturation ratio and critical size are 29.6 and 17, respectively. The idea of inferring the critical size from cluster appearance times is not in principle well-founded in the case that the critical cluster corresponding to the final monomer concentration (or other reference monomer concentration) is so small that clusters around the critical size appear when the monomer concentration is still substantially below the final value. As the critical size is not known beforehand, it cannot be concluded from the appearance time data if this is the case.

### 4.2.1. *Effect of the magnitude of external losses*

As the magnitude of external loss terms may vary in different conditions, we ran simulations using not only the value $10^{-3}\ \mathrm{s}^{-1}$, but also $5\times10^{-4}$ and $2\times10^{-3}\ \mathrm{s}^{-1}$ for the loss coefficient of all the clusters. The monomer source was set to the same set of values as before, and thus the final steady-state monomer concentration (and the critical size corresponding to it) differs from that of the previous sets of simulations. The results for all studied loss coefficients with a monomer source rate of $8.1\times10^{3}\ \mathrm{cm}^{-3}\ \mathrm{s}^{-1}$ corresponding to a steady-state saturation ratio at $S=30$ with a loss coefficient of $10^{-3}\ \mathrm{s}^{-1}$ are shown in Fig. 4. Panel (a) shows that the shape of the ($t_{\mathrm{app}}$, size)-curve is significantly affected when the magnitude of the loss term is varied while keeping all the other conditions constant. The higher the loss coefficient is, the faster the monomer concentration approaches the steady state value (the vertical dash-dotted lines mark the time at which 95% of the final value is reached), and also the faster the concentrations of the smallest cluster sizes reach 50% of their final value. As a result, for the smallest sizes AGR ($\Delta\mathrm{size}/\Delta t_{\mathrm{app}}$) is higher in the case of a higher loss coefficient. For larger sizes AGR and FGR (panel (b)) decrease as the loss coefficient increases. The difference between AGR and FGR also increases with an increasing loss

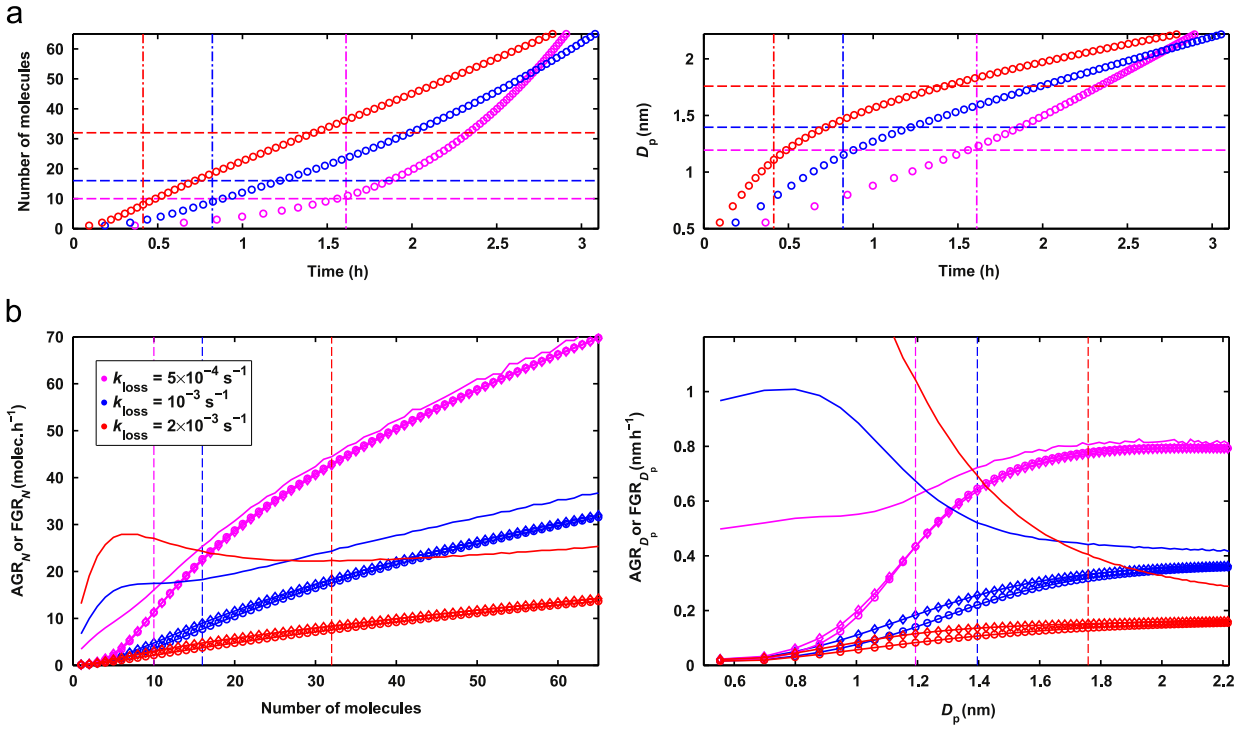


**Fig. 4.** Results for simulations with a constant monomer source rate of $8.1\times10^{3}\ \mathrm{cm}^{-3}\ \mathrm{s}^{-1}$ and external losses with a loss coefficient $k_{\mathrm{loss}}$ of $5\times10^{-4}$ (magenta), $10^{-3}\ \mathrm{s}^{-1}$ (blue) and $2\times10^{-3}\ \mathrm{s}^{-1}$ (red). Explanations for the panels are as for Fig. 2. Dashed lines mark the size of the critical cluster at the final steady state. The dash-dotted vertical lines in panel (a) mark the time at which the monomer concentration reaches 95% of its final value. (For interpretation of the references to color in this figure legend, the reader is referred to the web version of this article.)

coefficient. It must be noted, though, that if the monomer source rate in the simulations with different loss coefficients was fitted to produce the same final monomer concentration, the growth rates (both the flux-based FGR and the appearance time-based AGR) would increase with an increasing loss coefficient since (1) the evaporation flux would decrease as explained in Section 4.1, and (2) the needed monomer source rate would increase resulting in the clusters appearing generally faster. A time-dependent loss term – for example during a strong particle formation burst where a rapid increase in the concentration of freshly formed particles increases the coagulational scavenging sink for the smallest particles – may have a different effect on the cluster concentrations and appearance times.

### 4.2.2. Sinusoidal monomer concentration

In laboratory studies, the precursor vapor can be produced with a constant source rate for instance via a chemical reaction. In field measurements, however, the production rate of a vapor is most likely time-dependent. For instance, as atmospheric sulfuric acid is formed by the oxidation of sulfur dioxide by OH, its formation rate is dependent on the OH concentration, which in turn depends on solar radiation. This dependence can be roughly approximated by a sinusoidal sulfuric acid concentration that has a maximum around noon (as done, for example, by Sihto et al., 2009). Therefore, to study the time evolution of a cluster population in conditions corresponding to field measurements, the monomer concentration was set to have the form of sinusoidal function between 0 and $\pi$, with the minimum and maximum values equaling to representative initial and final monomer concentrations corresponding to $S_{\min}=0.1$ and $S_{\max}=30$ as in previous simulations. A loss coefficient of $10^{-3}\ s^{-1}$ was again used for all the clusters. To examine how the appearance times are affected by the rate at which the monomer concentration increases, the time difference between the minimum and maximum was set to 4, 6 and 8 h.

Figure 5b shows that while the growth rates for simulations with different time scales differ in absolute value, they behave rather similarly with respect to cluster size. As the timespan increases, AGR ($\Delta$size/$\Delta t_{\mathrm{app}}$; solid lines) decreases for all cluster sizes as the clusters appear with a reduced frequency. On the other hand, larger clusters appear and reach their maximum concentrations when the monomer concentration is already decreasing from its peak value. The later the cluster appears, the lower the monomer concentration and consequently the collision frequency of monomers is at that moment. Therefore, as the timespan increases, the monomer concentration decreases more slowly and consequently the flux-based FGR calculated at the appearance time or at the time of the maximum concentration of each cluster (diamonds and circles, respectively) increases for the larger sizes.

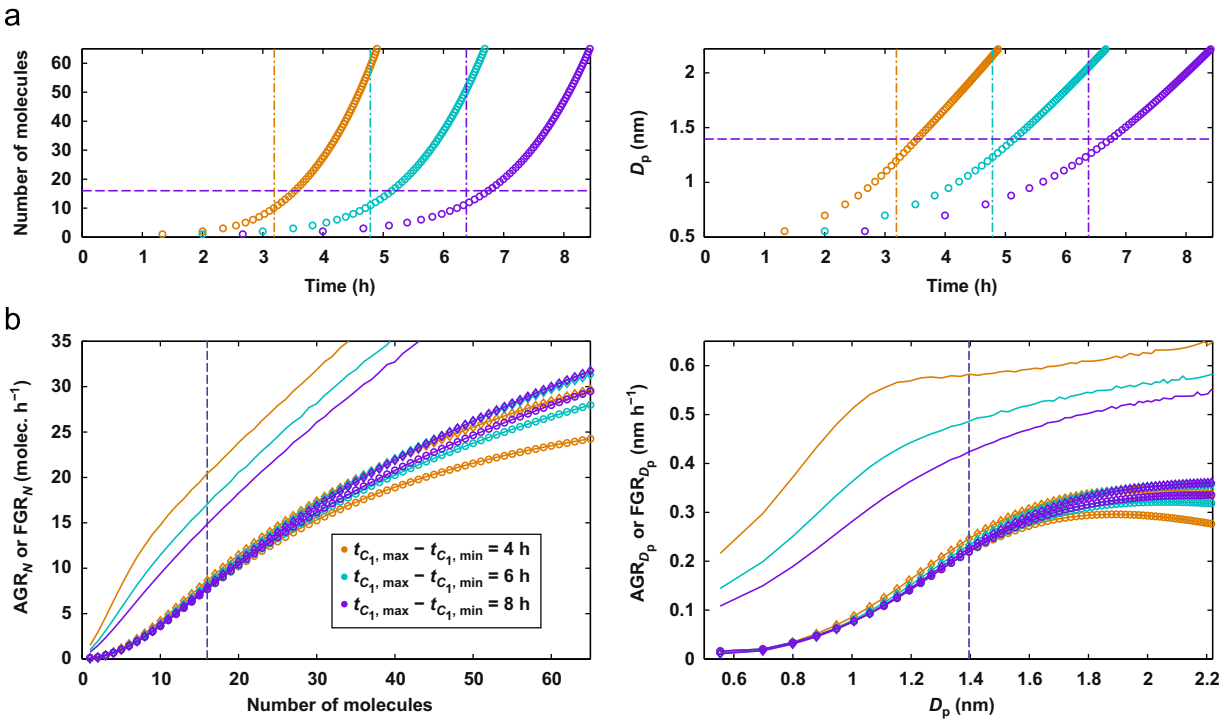


**Fig. 5.** Results for simulations with a sinusoidal monomer concentration with minimum and maximum values corresponding to saturation ratios of 0.1 and 30, respectively, and external losses with a loss coefficient of $10^{-3}\ s^{-1}$, with the time difference between the minimum and maximum $t_{c_1,\,max} - t_{c_1,\,min}$ set to 4 (orange), 6 (turquoise) and 8 (purple) hours. Explanations for the panels are as for Fig. 2, except that here the lines with circles present FGR calculated at the time when the clusters reach the maximum concentration. Dashed lines mark the size of the critical cluster at the maximum monomer concentration. The dash-dotted vertical lines in panel (a) mark the time at which the monomer concentration reaches 95% of its maximum value. (For interpretation of the references to color in this figure legend, the reader is referred to the web version of this article.)

Figure 5a shows that as the monomer increase rate is lowered, the time difference $\Delta t_{app}$ between the appearance of consecutive cluster sizes increases the most for the smallest clusters, altering the shape of the ($t_{app}$, size)-curve. This demonstrates that, in addition to other ambient conditions and cluster stabilities, also the time evolution of the monomer concentration affects the shape and slope of the ($t_{app}$, size)-curve. Again, it should be kept in mind that in this case the critical size is time-dependent. To better elucidate the effect of varying ambient conditions on the shape of the ($t_{app}$, size)-curve, the curves for all the case studies at a saturation ratio of $S=30$ are shown together in Fig. A3a in Appendix A.

## 5. Conclusions

We simulated the time development of molecular cluster concentrations with a cluster dynamics model in a system where the clusters grow by monomer additions, and the cluster formation free energy curve exhibits a single maximum corresponding to a critical cluster. For simplicity, the modeled molecules were set to have the mass, density and surface tension of liquid sulfuric acid, but the saturation vapor pressure of the model substance was adjusted to produce atmospherically relevant monomer concentrations and cluster evaporation rates that are in the range of those calculated from quantum chemical free energies for small sulfuric acid–base clusters. We determined the cluster growth rates from the time-dependent cluster concentrations (1) as the slope of the cluster size as a function of cluster appearance time (the time at which the increase in the cluster concentration reaches 50% of its maximum value) as in the experimental procedure, and (2) by calculating the net cluster flux along size axis from given cluster size to the subsequent size. The growth rate calculated from the molecular flux was determined both at the final steady state and at the appearance time of the cluster; in general there was no significant difference between the growth rates calculated at these different times. While first a hypothetical situation with a constant monomer concentration and no external cluster sinks was examined, the simulations were mainly performed using an increasing monomer concentration and external losses to pre-existing larger particles or chamber walls in order to mimic realistic conditions. The main conclusions can be summarized as follows:

(i) In the studied conditions, the growth rate determined from the appearance times is higher than the growth rate calculated from the molecular fluxes especially for the smallest cluster sizes, with the difference decreasing with increasing cluster size. For the model substance and conditions considered here, the ratio was found to approach the value ~1–2 for clusters larger than the critical size. For smaller clusters, the ratio increases up to ~10–100 with decreasing size, depending on the simulation conditions. The growth rates determined with the two methods are both affected by cluster evaporation, and thus their size-dependent ratio may be different for other substances with different evaporation profiles.
(ii) External loss terms slightly increase the growth rate compared to a situation with the same monomer concentration and no losses. This is due to changes in the cluster size distribution caused by the presence of external losses, resulting in reduced evaporation fluxes. If the magnitude of the external losses increases while all the other conditions are constant, the growth rates generally decrease, and the difference between the growth rates determined from the appearance times and the fluxes increases. However, for the smallest clusters the growth rate determined with the appearance time method increases because the cluster concentrations build up faster when losses are higher.
(iii) In realistic conditions where the monomer concentration increases simultaneously with the cluster concentrations and there are external sinks for the molecules and clusters, critical cluster size cannot be deduced from cluster growth rates by reasoning that clusters larger than the critical size grow faster than sub-critical clusters.
(iv) The appearance time-based and the flux-equivalent growth rates, as well as their ratio as a function of cluster size are not affected only by the collision and evaporation rates and other properties of the substance, but also by external conditions including the magnitude of loss terms and the time evolution of the monomer concentration. Therefore, even in the case of a simple substance with a classical evaporation profile, obtaining quantitative results for the relation of the growth rates determined with the two methods in specific situations requires studying each set of conditions separately.

Determining the growth rate in a situation where the growth involves significant contributions from collisions between two clusters is more complex, as the definition of growth rate is not unambiguous in such a case. Also, in practice the size resolution in particle measurements may not be as accurate as one molecule, but instead the clusters must be grouped into size classes. The effects of these practical details on the appearance time-based and flux-equivalent growth rates are the topic of future work.

## Acknowledgments

ERC Projects 257360-MOCAPAF and 278277-ATMOGAIN and the Academy of Finland Center of Excellence program Project no. 272041 are acknowledged for funding. The authors thank Oona Kupiainen-Määttä, Ville Loukonen, Jenni Kontkanen and Markku Kulmala for valuable discussions and useful comments.

## Appendix A

### A.1. Effect of evaporation fluxes

Figure A1 shows the growth rate FGR calculated from the net molecular flux (Eq. (7)), and the growth rate calculated neglecting the evaporation flux (that is, considering only the first term $\beta_{i,1}C_1$ in the last factor of Eq. (7) in the calculation) $FGR_{coll}$ (panel (a)) and their difference $FGR_{coll} - FGR$ (panel (b)) for the situations with a constant monomer concentration and no losses (Section 4.1, Fig. 2) and an increasing monomer concentration with external losses (Section 4.2, Fig. 3) for $S=30$. The monomer collision frequency at the steady state is same for both situations (and in the case of the constant monomer concentration, the collision frequency is the same at the steady state and at the mean appearance time $t_{app,\,mean}$). Also the growth rate AGR ($\Delta size/\Delta t_{app}$; Eq. (2)) determined from the appearance times, and the difference between the growth rate calculated from the collision frequency $FGR_{coll}$ at $t_{app,\,mean}$ and AGR are shown. Panel (b) explicitly shows that the contribution of evaporation flux is smaller in the case of a time-dependent monomer concentration and losses except for the smallest clusters at their appearance time $t_{app,\,mean}$, as discussed in Sections 4.1 and 4.2.

In general, Fig. A1 shows that evaporation flux may have a prominent effect on cluster growth rate also for sizes larger than the critical cluster. By definition, for the critical cluster the collision frequency with a monomer equals the monomer evaporation frequency (Fig. 1b). For clusters smaller than the critical size, the evaporation rate is higher than the condensation rate, and for clusters larger than the critical size, the condensation rate is higher – nevertheless, this does not imply that the larger clusters would not evaporate at all. In the studied conditions, the absolute contribution of evaporation flux to the net rate at which the cluster gains molecules is the highest at sizes around or below the critical cluster and decreases at larger sizes with increasing cluster size (lower left-hand side panel of Fig. A1). The contribution to the cluster

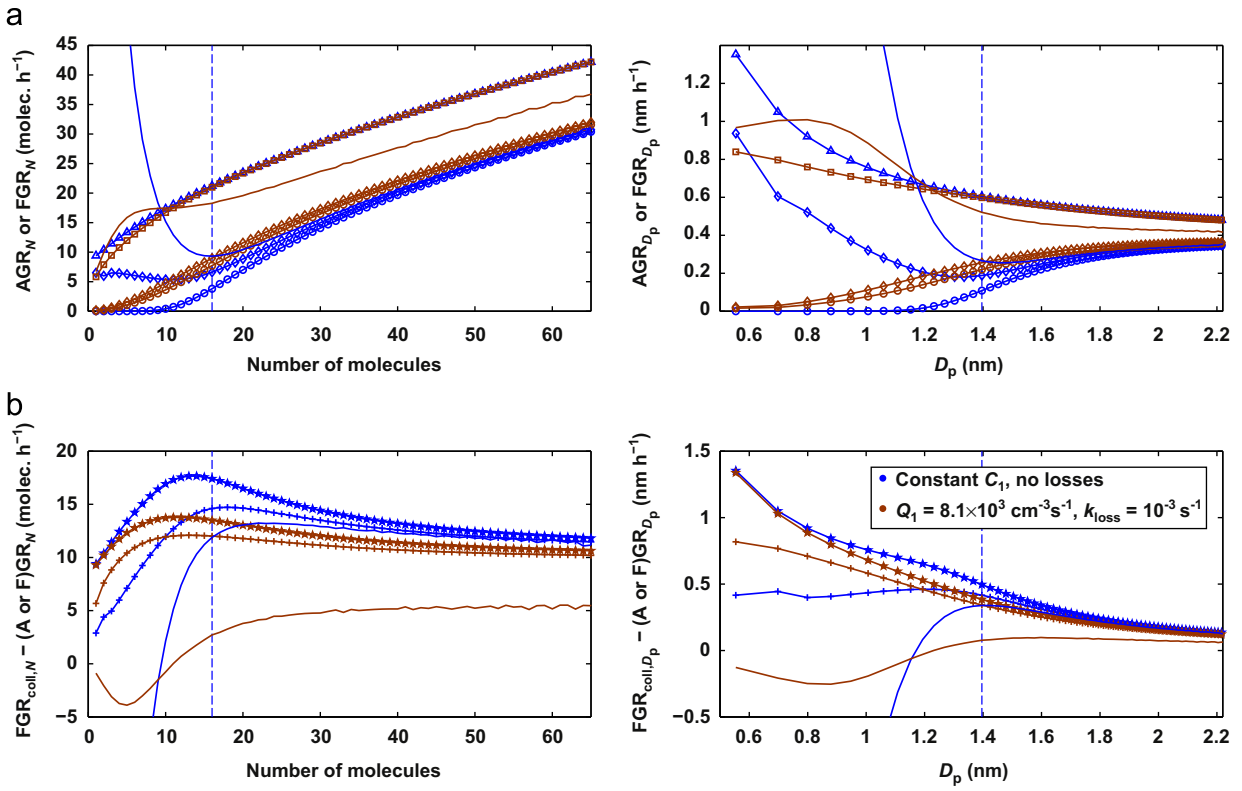


**Fig. A1.** Results for simulations with a constant monomer concentration corresponding to a saturation ratio $S=30$ and no external losses (blue), and for simulations with a constant monomer source rate corresponding to a steady-state saturation ratio $S=30$ and external losses with a loss coefficient of $10^{-3}$ s$^{-1}$ (brown). Panel (a): Molecular flux-based cluster growth rate as a function of cluster size calculated (1) from the net flux onto the cluster (FGR) at the steady-state (lines with circles) and at the appearance time $t_{app,\,mean}$ (lines with diamonds), and (2) from the collision flux neglecting evaporation ($FGR_{coll}$) at the steady-state (lines with triangles) and at the appearance time $t_{app,\,mean}$ (lines with squares), and the growth rate determined from the appearance times (AGR; solid lines). Panel (b): The difference between the molecular growth rate calculated from the collision flux and from the net flux at the steady-state (lines with stars) and at the appearance time $t_{app,\,mean}$ (lines with plus signs), and the difference between the molecular growth rate calculated from the collision flux at $t_{app,\,mean}$ and the growth rate determined from the appearance times (solid lines). Dashed lines mark the size of the critical cluster at the final steady state. Cluster size and growth rate are given as the number of molecules in the left-hand panels, and as the mass diameter in the right-hand panels. (For interpretation of the references to color in this figure legend, the reader is referred to the web version of this article.)

diameter growth rate is not as straightforward: for this simple one-component system, the diameter growth rate calculated from the collision flux actually decreases as a function of cluster size (upper right-hand side panel). Although the collision frequency with monomers increases with the cluster diameter, the change in the diameter due to addition of one molecule (the pre-factor $D_{p,i+1}-D_{p,i}$ in Eq. (7)) decreases, causing the overall decreasing effect. Therefore, the absolute contribution of evaporation flux to the diameter growth rate is highest for the smallest clusters for which the diameter change per added molecule is the largest (lower right-hand side panel).

Since measurements provide the apparent growth rate resulting from the net molecular fluxes, the contribution of evaporation fluxes has been assessed by comparing the observed growth rate to theoretical growth rate calculated assuming irreversible vapor condensation (Kuang et al., 2012; Kulmala et al., 2013). In the conditions studied here, comparing the measurable growth rate AGR determined from the appearance times to the growth rate calculated from the monomer collision frequency $FGR_{coll}$ would lead to an underestimation of the contribution of evaporation (solid lines in panel (b) of Fig. A1), as the growth rate obtained from the appearance times is in general higher than the growth rate FGR calculated from the net collision–evaporation flux. If it is assumed that sizes for which the observed growth rate is lower than the calculated condensational growth rate $FGR_{coll}$ are likely to be sub-critical, the fact that the contribution of evaporation is non-zero also above the critical cluster would result in wrong estimates of the critical size. On the other hand, for the smallest clusters below the critical size (dashed lines in Fig. A1) the measurable growth rate AGR (solid lines in panel (a)) may exceed the collision-limited growth rate $FGR_{coll}$ (lines with triangles and squares corresponding to the steady state and $t_{app,\ mean}$, respectively, in panel (a)). In this case, comparing the measurable growth rate to $FGR_{coll}$ would lead to the erroneous conclusion that these small clusters are likely to be larger than the critical size.

### A.2. Time evolution of the flux-equivalent growth rate

Figure A2 shows FGR as a function of time for a representative set of cluster sizes for the case studies presented in Sections 4.1. and 4.2 (solid and dashed lines, respectively) at $S=30$. The mean appearance time $t_{app,\ mean}$ of each cluster is marked on its growth rate curve with a symbol (circle for solid lines and cross for dashed lines). In the case of a constant monomer concentration and no losses (Sections 4.1; solid lines), FGR decreases as a function of time for each cluster, because concentrations of larger clusters, and consequently evaporation fluxes from them increase. For an increasing monomer concentration and external losses (Section 4.2; dashed lines), FGR first slightly increases as the monomer concentration increases, and then decreases with increasing evaporation fluxes. (See also discussion in Section 4.1 and 4.2.)

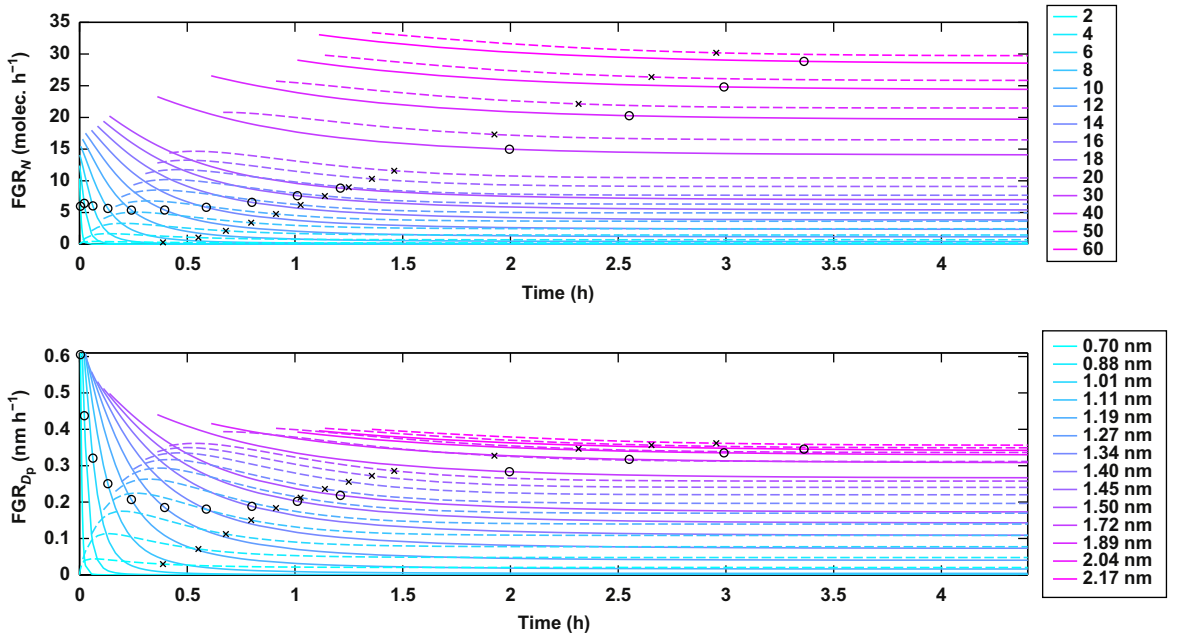


**Fig. A2.** Flux-equivalent growth rate FGR as a function of time for a representative set of clusters for simulations with a constant monomer concentration corresponding to a saturation ratio $S=30$ and no external losses (solid lines), and for simulations with a constant monomer source rate corresponding to a steady-state saturation ratio $S=30$ and external losses with a loss coefficient of $10^{-3}\ s^{-1}$ (dashed lines). The growth rate of each cluster is calculated starting from the time at which the concentration of the cluster reaches $10^{-6}$ times the final value. The symbol (circle for solid lines and cross for dashed lines) on each growth rate curve marks the mean appearance time $t_{app,\ mean}$. Cluster size and growth rate are given as the number of molecules in the top panel, and as the mass diameter in the bottom panel.

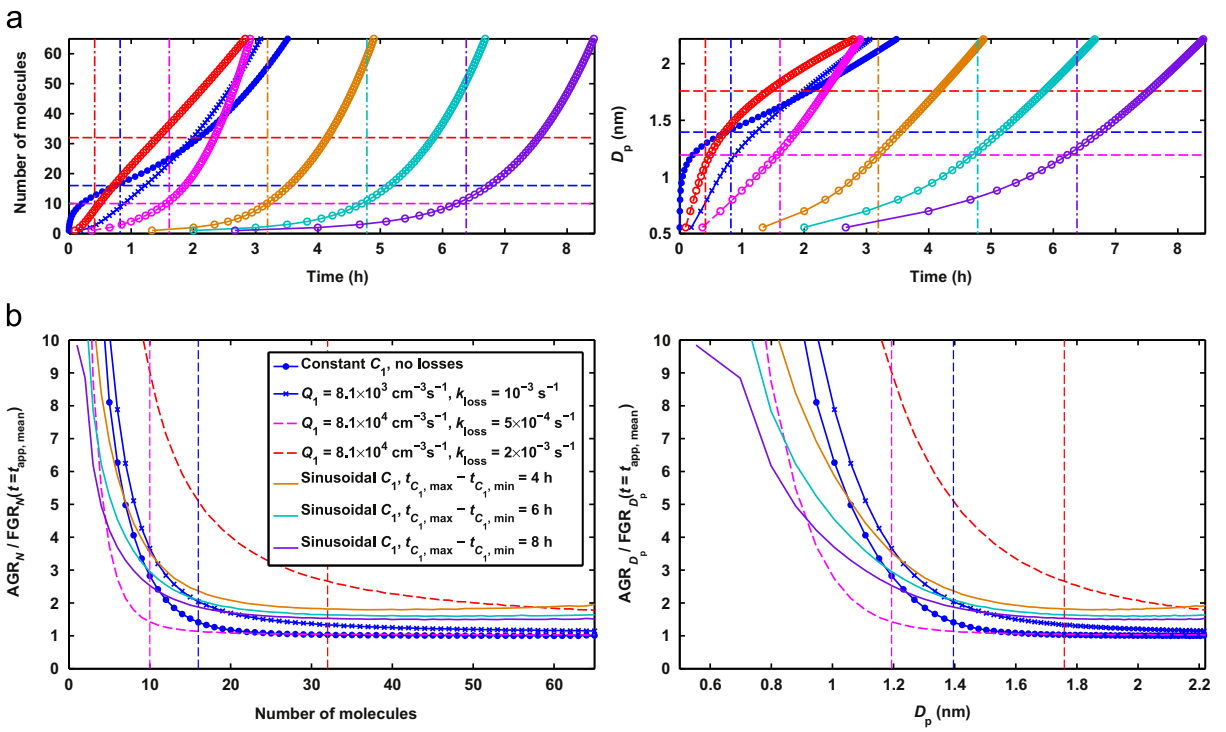


**Fig. A3.** Results for the case studies presented in Sections 4.1 and 4.2 (Figs. 2–5) for a representative final (or maximum in the case of the sinusoidal monomer concentration) saturation ratio $S=30$ or monomer source rate $Q_1=8.1\times10^3$ cm$^{-3}$ s$^{-1}$ (in the case of the varying external loss coefficient $k_{loss}$). Panel (a): Cluster size as a function of appearance time. Panel (b): Ratio of the growth rate AGR determined from the appearance times and the molecular flux-based growth rate FGR calculated at $t_{app,\ mean}$. Dashed lines (horizontal lines in panel (a) and vertical lines in panel (b)) mark the size of the critical cluster at the final or maximum $S$ (the magenta and red lines correspond to the case with varying $k_{loss}$, for which the final saturation ratios are different, and the blue line corresponds to all other cases). In panel (a), the vertical dash-dotted lines mark the time at which the monomer concentration reaches 95% of its final (or maximum) value. Cluster size and growth rate are given as the number of molecules in the left-hand panels, and as the mass diameter in the right-hand panels. (For interpretation of the references to color in this figure legend, the reader is referred to the web version of this article.)

### *A.3. Effect of simulation conditions on the appearance times and on the ratios of the growth rates determined with the different methods*

Figure A3 shows the ($t_{app}$, size)-curve and the ratio of the apparent growth rate AGR and the flux-based growth rate FGR calculated at $t_{app,\ mean}$ for all the studied conditions at a representative final or maximum saturation ratio $S=30$, or monomer source rate $8.1\times10^3$ cm$^{-3}$ s$^{-1}$ in the case of a varying external loss coefficient. The effect of simulation conditions is largest for the small clusters: their relative appearance times may vary significantly with the magnitude of external losses (blue crosses and magenta and red circles in panel (a)) or the increase rate of the monomer concentration (orange, turquoise and purple circles in panel (a)). For small sub-critical clusters, the ratio AGR/FGR ($t=t_{app,\ mean}$) increases up to ~10–90 as the cluster size decreases depending on the conditions (panel (b)). For larger clusters, the ratio is circa 1–2 in the considered conditions. This suggests that the sensitivity of the appearance time method to ambient conditions is high for very small clusters. The ratio as a function of cluster size (panel (b)) is qualitatively similar for the other saturation ratios $S=20$ and 40 used in this study, but the absolute values are generally higher for lower $S$. For instance, for $S=20$ the ratio increases to values over 100 in the conditions of Fig. A3. However, the ratio as a function of cluster size depends also on cluster evaporation rates, and may thus be significantly different for substances with different evaporation profiles.

## References

Almeida, J., Schobesberger, S., Kürten, A., Ortega, I.K., Kupiainen-Määttä, O., Praplan, A.P., Adamov, A., Amorim, A., Bianchi, F., Breitenlechner, M., David, A., Dommen, J., Donahue, N.M., Downard, A., Dunne, E., Duplissy, J., Ehrhart, S., Flagan, R.C., Franchin, A., Guida, R., Hakala, J., Hansel, A., Heinritzi, M., Henschel, H., Jokinen, T., Junninen, H., Kajos, M., Kangasluoma, J., Keskinen, H., Kupc, A., Kurtén, T., Kvashin, A.N., Laaksonen, A., Lehtipalo, K., Leiminger, M., Leppä, J., Loukonen, V., Makhmutov, V., Mathot, S., McGrath, M.J., Nieminen, T., Olenius, T., Onnela, A., Petäjä, T., Riccobono, F., Riipinen, I., Rissanen, M., Rondo, L., Ruuskanen, T., Santos, F.D., Sarnela, N., Schallhart, S., Schnitzhofer, R., Seinfeld, J.H., Simon, M., Sipilä, M., Stozhkov, Y., Stratmann, F., Tomé, A., Tröstl, J., Tsagkogeorgas, G., Vaattovaara, P., Viisanen, Y., Virtanen, A., Vrtala, A., Wagner, P.E., Weingartner, E., Wex, H., Williamson, C., Wimmer, D., Ye, P., Yli-Juuti, T., Carslaw, K.S., Kulmala, M., Curtius, J., Baltensperger, U., Worsnop, D.R., Vehkamäki, H., & Kirkby, J. (2013). Molecular understanding of sulphuric acid-amine particle nucleation in the atmosphere. *Nature*, *502*, 359–363.

Dal Maso, M., Hyvärinen, A., Komppula, M., Tunved, P., Kerminen, V.-M., Lihavainen, H., Viisanen, Y., Hansson, H.-C., & Kulmala, M. (2008). Annual and interannual variation in boreal forest aerosol particle number and volume concentration and their connection to particle formation. *Tellus, Series B: Chemical and Physical Meteorology*, *60*, 495–508.

Dal Maso, M., Kulmala, M., Riipinen, I., Wagner, R., Hussein, T., Aalto, P.P., & Lehtinen, K.E. J. (2005). Formation and growth of fresh atmospheric aerosols: eight years of aerosol size distribution data from SMEAR II, Hyytiälä, Finland. *Boreal Environment Research*, *10*, 323–336.

Fiedler, V., Dal Maso, M., Boy, M., Aufmhoff, H., Hoffmann, J., Schuck, T., Birmili, W., Hanke, M., Uecker, J., Arnold, F., & Kulmala, M. (2005). The contribution of sulphuric acid to atmospheric particle formation and growth: a comparison between boundary layers in northern and central Europe. *Atmospheric Chemistry and Physics*, *5*, 1773–1785.

Fuchs, N.A., & Sutugin, A.G. (1970). *Highly Dispersed Aerosols*. Ann Arbor Science Publisher: Ann Arbor.

Hirsikko, A., Laakso, L., Hõrrak, U., Aalto, P.P., Kerminen, V.-M., & Kulmala, M. (2005). Annual and size dependent variation of growth rates and ion concentrations in boreal forest. *Boreal Environment Research*, *10*, 357–369.

Jiang, J., Chen, M., Kuang, C., Attoui, M., & McMurry, P.H. (2011). Electrical mobility spectrometer using a diethylene glycol condensation particle counter for measurement of aerosol size distributions down to 1 nm. *Aerosol Science and Technology*, *45*, 510–521.

Junninen, H., Ehn, M., Petäjä, T., Luosujärvi, L., Kotiaho, T., Kostiainen, R., Rohner, U., Gonin, M., Fuhrer, K., Kulmala, M., & Worsnop, D.R. (2010). A high-resolution mass spectrometer to measure atmospheric ion composition. *Atmospheric Measurement Techniques*, *3*, 1039–1053.

Kerminen, V.-M., Pirjola, L., & Kulmala, M. (2001). How significantly does coagulational scavenging limit atmospheric particle production?. *Journal of Geophysical Research D: Atmospheres*, *106*, 24119–24125.

Kirkby, J., Curtius, J., Almeida, J., Dunne, E., Duplissy, J., Ehrhart, S., Franchin, A., Gagné, S., Ickes, L., Kürten, A., Kupc, A., Metzger, A., Riccobono, F., Rondo, L., Schobesberger, S., Tsagkogeorgas, G., Wimmer, D., Amorim, A., Bianchi, F., Breitenlechner, M., David, A., Dommen, J., Downard, A., Ehn, M., Flagan, R.C., Haider, S., Hansel, A., Hauser, D., Jud, W., Junninen, H., Kreissl, F., Kvashin, A., Laaksonen, A., Lehtipalo, K., Lima, J., Lovejoy, E.R., Makhmutov, V., Mathot, S., Mikkilä, J., Minginette, P., Mogo, S., Nieminen, T., Onnela, A., Pereira, P., Petäjä, T., Schnitzhofer, R., Seinfeld, J.H., Sipilä, M., Stozhkov, Y., Stratmann, F., Tomé, A., Vanhanen, J., Viisanen, Y., Vrtala, A., Wagner, P.E., Walther, H., Weingartner, E., Wex, H., Winkler, P.M., Carslaw, K.S., Worsnop, D.R., Baltensperger, U., & Kulmala, M. (2011). Role of sulphuric acid, ammonia and galactic cosmic rays in atmospheric aerosol nucleation. *Nature*, *476*, 429–433.

Kuang, C., Chen, M., Zhao, J., Smith, J., McMurry, P.H., & Wang, J. (2012). Size and time-resolved growth rate measurements of 1 to 5 nm freshly formed atmospheric nuclei. *Atmospheric Chemistry and Physics*, *12*, 3573–3589.

Kuang, C., McMurry, P.H., McCormick, A.V., & Eisele, F.L. (2008). Dependence of nucleation rates on sulfuric acid vapor concentration in diverse atmospheric locations. *Journal of Geophysical Research*, *113*, D10209, http://dx.doi.org/10.1029/2007JD009253.

Kuang, C., Riipinen, I., Sihto, S.-L., Kulmala, M., McCormick, A.V., & McMurry, P.H. (2010). An improved criterion for new particle formation in diverse atmospheric environments. *Atmospheric Chemistry and Physics*, *10*, 8469–8480.

Kulmala, M., Kontkanen, J., Junninen, H., Lehtipalo, K., Manninen, H.E., Nieminen, T., Petäjä, T., Sipilä, M., Schobesberger, S., Rantala, P., Franchin, A., Jokinen, T., Järvinen, E., Äijälä, M., Kangasluoma, J., Hakala, J., Aalto, P.P., Paasonen, P., Mikkilä, J., Vanhanen, J., Aalto, J., Hakola, H., Makkonen, U., Ruuskanen, T., Mauldin, R.L., III, Duplissy, J., Vehkamäki, H., Bäck, J., Kortelainen, A., Riipinen, I., Kurtén, T., Johnston, M.V., Smith, J.N., Ehn, M., Mentel, T.F., Lehtinen, K.E. J., Laaksonen, A., Kerminen, V.-M., & Worsnop, D.R. (2013). Direct observations of atmospheric aerosol nucleation. *Science*, *339*, 943–946, http://dx.doi.org/10.1126/science.1227385.

Kulmala, M., Petäjä, T., Nieminen, T., Sipilä, M., Manninen, H.E., Lehtipalo, K., Dal Maso, M., Aalto, P.P., Junninen, H., Paasonen, P., Riipinen, I., Lehtinen, K.E. J., Laaksonen, A., & Kerminen, V.-M. (2012). Measurement of the nucleation of atmospheric aerosol particles. *Nature Protocols*, *7*, 1651–1667.

Larriba, C., Hogan, C.J., Jr., Attoui, M., Borrajo, R., Garcia, J.F., & De La Mora, J.F. (2011). The mobility–volume relationship below 3.0 nm examined by tandem mobility–mass measurement. *Aerosol Science and Technology*, *45*, 453–467.

Lehtinen, K.E. J., Rannik, Ü., Petäjä, T., Kulmala, M., & Hari, P. (2004). Nucleation rate and vapor concentration estimations using a least squares aerosol dynamics method. *Journal of Geophysical Research D: Atmospheres*, *109*(D21209), 1–5.

Lehtipalo, K., Leppä, J., Kontkanen, J., Kangasluoma, J., Franchin, A., Wimmer, D., Schobesberger, S., Junninen, H., Petäjä, T., Sipilä, M., Mikkilä, J., Vanhanen, J., Worsnop, D.R., & Kulmala, M. (2014). Methods for determining particle size distribution and growth rates between 1 and 3 nm using the Particle Size Magnifier. *Boreal Environment Research*, *19* (*Suppl. B*), 215–S236.

Leppä, J., Anttila, T., Kerminen, V.-M., Kulmala, M., & Lehtinen, K.E. J. (2011). Atmospheric new particle formation: real and apparent growth of neutral and charged particles. *Atmospheric Chemistry and Physics*, *11*, 4939–4955.

Manninen, H.E., Nieminen, T., Asmi, E., Gagné, S., Häkkinen, S., Lehtipalo, K., Aalto, P., Vana, M., Mirme, A., Mirme, S., Hõrrak, U., Plass-Dülmer, C., Stange, G., Kiss, G., Hoffer, A., Töro, N., Moerman, M., Henzing, B., De Leeuw, G., Brinkenberg, M., Kouvarakis, G.N., Bougiatioti, A., Mihalopoulos, N., O'Dowd, C., Ceburnis, D., Arneth, A., Svenningsson, B., Swietlicki, E., Tarozzi, L., Decesari, S., Facchini, M.C., Birmili, W., Sonntag, A., Wiedensohler, A., Boulon, J., Sellegri, K., Laj, P., Gysel, M., Bukowiecki, N., Weingartner, E., Wehrle, G., Laaksonen, A., Hamed, A., Joutsensaari, J., Petäjä, T., Kerminen, V.-M., & Kulmala, M. (2010). EUCAARI ion spectrometer measurements at 12 European sites—analysis of new particle formation events. *Atmospheric Chemistry and Physics*, *10*, 7907–7927.

Manninen, H.E., Nieminen, T., Riipinen, I., Yli-Juuti, T., Gagné, S., Asmi, E., Aalto, P.P., Petäjä, T., Kerminen, V.-M., & Kulmala, M. (2009). Charged and total particle formation and growth rates during EUCAARI 2007 campaign in Hyytiälä. *Atmospheric Chemistry and Physics*, *9*, 4077–4089.

McGrath, M.J., Olenius, T., Ortega, I.K., Loukonen, V., Paasonen, P., Kurtén, T., Kulmala, M., & Vehkamäki, H. (2012). Atmospheric cluster dynamics code: a flexible method for solution of the birth–death equations. *Atmospheric Chemistry and Physics*, *12*, 2345–2355, http://dx.doi.org/10.5194/acp-12-2345-2012.

Nieminen, T., Lehtinen, K.E. J., & Kulmala, M. (2010). Sub-10 nm particle growth by vapor condensation—effects of vapor molecule size and particle thermal speed. *Atmospheric Chemistry and Physics*, *10*, 9773–9779.

Olenius, T., Kupiainen-Määttä, O., Ortega, I.K., Kurtén, T., & Vehkamäki, H. (2013). Free energy barrier in the growth of sulfuric acid–ammonia and sulfuric acid–dimethylamine clusters. *Journal of Chemical Physics*, *139*, 084312.

Ortega, I.K., Kupiainen, O., Kurtén, T., Olenius, T., Wilkman, O., McGrath, M.J., Loukonen, V., & Vehkamäki, H. (2012). From quantum chemical formation free energies to evaporation rates. *Atmospheric Chemistry and Physics*, *12*, 225–235, http://dx.doi.org/10.5194/acp-12-225-2012.

Ouyang, H., Larriba-Andaluz, C., Oberreit, D.R., & Hogan, C.J. (2013). The collision cross sections of iodide salt cluster ions in air via differential mobility analysis-mass spectrometry. *Journal of the American Society for Mass Spectrometry*, *24*, 1833–1847.

Pierce, J.R., Riipinen, I., Kulmala, M., Ehn, M., Petäjä, T., Junninen, H., Worsnop, D.R., & Donahue, N.M. (2011). Quantification of the volatility of secondary organic compounds in ultrafine particles during nucleation events. *Atmospheric Chemistry and Physics*, *11*, 9019–9036.

Riccobono, F., Rondo, L., Sipilä, M., Barmet, P., Curtius, J., Dommen, J., Ehn, M., Ehrhart, S., Kulmala, M., Kürten, A., Mikkilä, J., Paasonen, P., Petäjä, T., Weingartner, E., & Baltensperger, U. (2012). Contribution of sulfuric acid and oxidized organic compounds to particle formation and growth. *Atmospheric Chemistry and Physics*, *12*, 9427–9439.

Riipinen, I., Yli-Juuti, T., Pierce, J.R., Petäjä, T., Worsnop, D.R., Kulmala, M., & Donahue, N.M. (2012). The contribution of organics to atmospheric nanoparticle growth. *Nature Geoscience*, *5*, 453–458.

Schobesberger, S., Junninen, H., Bianchi, F., Lönn, G., Ehn, M., Lehtipalo, K., Dommen, J., Ehrhart, S., Ortega, I.K., Franchin, A., Nieminen, T., Riccobono, F., Hutterli, M., Duplissy, J., Almeida, J., Amorim, A., Breitenlechner, M., Downard, A.J., Dunne, E.M., Flagan, R.C., Kajos, M., Keskinen, H., Kirkby, J., Kupc, A., Kürten, A., Kurtén, T., Laaksonen, A., Mathot, S., Onnela, A., Praplan, A.P., Rondo, L., Santos, F.D., Schallhart, S., Schnitzhofer, R., Sipilä, M., Tomé, A., Tsagkogeorgas, G., Vehkamäki, H., Wimmer, D., Baltensperger, U., Carslaw, K.S., Curtius, J., Hansel, A., Petäjä, T., Kulmala, M., Donahue, N.M., & Worsnop, D.R. (2013). Molecular understanding of atmospheric particle formation from sulfuric acid and large oxidized organic molecules. *Proceedings of the National Academy of Sciences of the United States of America*, *110*, 17223–17228.

Shampine, L., & Reichelt, M. (1997). The MATLAB ODE suite. *SIAM Journal on Scientific Computing*, *18*, 1–22, http://dx.doi.org/10.1137/S1064827594276424.

Sihto, S.-L., Kulmala, M., Kerminen, V.-M., Dal Maso, M., Petäjä, T., Riipinen, I., Korhonen, H., Arnold, F., Janson, R., Boy, M., Laaksonen, A., & Lehtinen, K.E. J. (2006). Atmospheric sulphuric acid and aerosol formation: implications from atmospheric measurements for nucleation and early growth mechanisms. *Atmospheric Chemistry and Physics*, *6*, 4079–4091, http://dx.doi.org/10.5194/acp-6-4079-2006.

Sihto, S.-L., Vuollekoski, H., Leppä, J., Riipinen, I., Kerminen, V.-M., Korhonen, H., Lehtinen, K.E. J., Boy, M., & Kulmala, M. (2009). Aerosol dynamics simulations on the connection of sulphuric acid and new particle formation. *Atmospheric Chemistry and Physics*, *9*, 2933–2947.

Stolzenburg, M.R., McMurry, P.H., Sakurai, H., Smith, J.N., Mauldin, R.L., III, Eisele, F.L., & Clement, C.F. (2005). Growth rates of freshly nucleated atmospheric particles in Atlanta. *Journal of Geophysical Research D: Atmospheres*, *110*, 1–10.

Vanhanen, J., Mikkilä, J., Lehtipalo, K., Sipilä, M., Manninen, H.E., Siivola, E., Petäjä, T., & Kulmala, M. (2011). Particle size magnifier for nano-CN detection. *Aerosol Science and Technology*, *45*, 533–542.

Verheggen, B., & Mozurkewich, M. (2006). An inverse modeling procedure to determine particle growth and nucleation rates from measured aerosol size distributions. *Atmospheric Chemistry and Physics*, *6*, 2927–2942.

Weber, R.J., Marti, J.J., McMurry, P.H., Eisele, F.L., Tanner, D.J., & Jefferson, A. (1997). Measurements of new particle formation and ultrafine particle growth rates at a clean continental site. *Journal of Geophysical Research D: Atmospheres*, *102*, 4375–4385.

Wimmer, D., Lehtipalo, K., Nieminen, T., Duplissy, J., Ehrhart, S., Almeida, J., Rondo, L., Franchin, A., Kreissl, F., Manninen, H.E., Kulmala, M., Curtius, J., & Petäjä, T. (2014). Technical note: using DEG CPCs at upper tropospheric temperatures. *Atmospheric Chemistry and Physics Discussions*, *14*, 12797–12817, http://dx.doi.org/10.5194/acpd-14-12797-2014.

Wu, D.T. (1992). The time lag in nucleation theory. *Journal of Chemical Physics*, *97*, 2644–2650.

Yli-Juuti, T., Barsanti, K., Hildebrandt Ruiz, L., Kieloaho, A.-J., Makkonen, U., Petäjä, T., Ruuskanen, T., Kulmala, M., & Riipinen, I. (2013). Model for acid–base chemistry in nanoparticle growth (MABNAG). *Atmospheric Chemistry and Physics*, *13*, 12507–12524.

Yli-Juuti, T., Nieminen, T., Hirsikko, A., Aalto, P.P., Asmi, E., Hõrrak, U., Manninen, H.E., Patokoski, J., Dal Maso, M., Petäjä, T., Rinne, J., Kulmala, M., & Riipinen, I. (2011). Growth rates of nucleation mode particles in Hyytiälä during 2003–2009: variation with particle size, season, data analysis method and ambient conditions. *Atmospheric Chemistry and Physics*, *11*, 12865–12886.

Yu, H., McGraw, R., & Lee, S.-H. (2012). Effects of amines on formation of sub-3 nm particles and their subsequent growth. *Geophysical Research Letters*, *39*, L02807.

Zhang, R., Suh, I., Zhao, J., Zhang, D., Fortner, E.C., Tie, X., Molina, L.T., & Molina, M.J. (2004). Atmospheric new particle formation enhanced by organic acids. *Science*, *304*, 1487–1490.